Hong-Sik Im[1]
Mem. ASME

Ge-Cheng Zha
Professor
e-mail: gzha@miami.edu

Bertrand P. E. Dano
Adjunct Faculty
Mem. ASME

Dept. of Mechanical and Aerospace Engineering,
University of Miami,
Coral Gables, FL 33124

Large Eddy Simulation of Coflow Jet Airfoil at High Angle of Attack

Large eddy simulation (LES) is conducted to investigate coflow jet (CFJ) airfoil flows at high angle of attack (AOA). The Smagorinsky model with Van Driest damping is employed to resolve the subgrid-scale stress. The fifth-order weighted essentially non-oscillatory (WENO) scheme is used for reconstruction of the inviscid flux and the fourth-order central differencing for the viscous flux. The LES results at an AOA of 0 deg, 12 deg, 25 deg, and 30 deg with momentum coefficients of $C_\mu = 0.15$ and 0.08 are compared with the experiment to understand the flow structure of the jet mixing and flow separation. The quantitative prediction of lift and drag and qualitative prediction of vortex structures are in good agreement with experiment. [DOI: 10.1115/1.4025649]

1 Introduction

The coflow jet (CFJ) flow control airfoil [1–4] for lift enhancement and drag reduction is designed with an injection slot near the leading edge and a suction slot near the trailing edge. The jet having high energy is injected tangentially near the leading edge and the same amount of mass flow is sucked in near the trailing edge to form a zero-net mass-flux flow control. The transport of energy from the jet to the main flow allows the main flow to overcome a severe adverse pressure gradient and remain attached at a high angle of attack. The high energy jet induces high circulation and, hence, generates high lift. The energized main flow fills the wake and, therefore, reduces drag. At low angle of attack, the drag reduction is often so great that a thrust or negative drag is created. The CFJ airfoil appears to be a very promising flow control technique to provide a drastic performance enhancement with low energy expenditure [5].

One challenge for numerical simulation of CFJ flow control airfoil using the Reynolds-averaged Navier–Stokes (RANS) model is that both C_L and C_D are significantly underpredicted at high angle of attack when the jet is not strong enough and the flow is separated [6]. Wang and Zha [7] improved the prediction at high angle of attack by using detached eddy simulation, which is a hybrid turbulence modeling using RANS near walls within boundary layers and large eddy simulation (LES) away from the walls. However, the lift and drag are still significantly underpredicted.

LES is an intermediate approach between direct numerical simulation (DNS) of turbulence and RANS. DNS has largely been limited to simple geometries at low Reynolds number due to excessive computing power needed since it requires grid points $\simeq \mathrm{Re}^{9/4}$ and times steps $\simeq \mathrm{Re}^{3/4}$ to resolve all scales of turbulence [8]. In LES, momentum and energy transfer of the large energy-carrying structures is computed directly and only the effect of the small scales of turbulence is modeled. A general model for small-scale structure is more plausible.

LES has been used for airfoil stall flows [9–11]. For example, Moreau et al. [11] employed LES to simulate trailing edge flow and noise of NACA0012 airfoil at near stall. It is pointed out in Ref. [11] that RANS fails to capture the stall point, while LES provides a more realistic behavior and qualitatively resolves better the shear layer and the von Kármán instabilities [11].

Recently, the experiment of the CFJ airfoil was conducted to investigate the CFJ airfoil mixing process [12]. The flow visualization was achieved by using digital particle image velocimetry and also the aerodynamic forces including lift and drag were measured. This is a completely different CFJ airfoil from the previous studies [1–4,7], which has a 25% thickness. The current airfoil has a 15% thickness for subsonic and transonic aircraft application. In this study, LES is utilized to simulate the flows of the CFJ airfoil experiment at various AOAs and the jet momentum coefficient C_μ of 0.15 and 0.08.

The purpose of this research is twofold: (1) using LES to further improve the prediction of lift and drag of CFJ airfoil at high angle of attack, and (2) using LES to study the fundamental mixing mechanism of the CFJ airfoil. A low diffusion energy-convection upstream split pressure (E-CUSP) scheme [13] is used with fifth-order weighted essentially non-oscillatory (WENO) reconstruction scheme [14] for the inviscid flux and fourth-order central differencing is used for the viscous flux [15]. The standard Smagorinsky model with Van Driest damping is adopted to model the subgrid-scale stress. The parallel computation is implemented with high scalability [16].

2 Spatially Filtered Compressible Navier–Stokes Equations

The governing equations are the spatially filtered full 3D Navier–Stokes equations, which eliminates the small-scale high frequency components of the fluid motion, while keeping the unsteadiness associated with the large-scale turbulent motion. For an arbitrary function $u(x_i, t)$, the filtered variable $\bar{u}(x_i, t)$ is defined as

$$\bar{u}(x_i, t) = \int_D G(x_i - \xi_i, \Delta) u(\xi_i, t) d\xi_i \tag{1}$$

where G is the filter function and Δ is the filter width and is associated with the mesh size. Similar to the case of RANS, for compressible flows, it is convenient to introduce the Favre-filtered variable $\tilde{u}(x_i, t)$ as

$$\tilde{u}(x_i, t) = \frac{\overline{\rho u}}{\bar{\rho}} \tag{2}$$

A variable can be, thus, decomposed into its Favre-filtered component and fluctuating component as

$$u(x_i, t) = \tilde{u}(x_i, t) + u''(x_i, t) \tag{3}$$

[1]Currently at Honeywell, Torrance CA 90505.

Contributed by the Fluids Engineering Division of ASME for publication in the Journal of Fluids Engineering. Manuscript received April 15, 2013; final manuscript received September 6, 2013; published online November 12, 2013. Assoc. Editor: Zvi Rusak.

Applying these definitions and following the derivation of Knight et al. [17], the filtered compressible Navier–Stokes(NS) equations in Cartesian coordinates can be expressed as

$$\frac{\partial \mathbf{Q}}{\partial t}+\frac{\partial \mathbf{E}}{\partial x}+\frac{\partial \mathbf{F}}{\partial y}+\frac{\partial \mathbf{G}}{\partial z}=\frac{1}{\mathrm{Re}}\left(\frac{\partial \mathbf{R}}{\partial x}+\frac{\partial \mathbf{S}}{\partial y}+\frac{\partial \mathbf{T}}{\partial z}\right) \tag{4}$$

where Re is the Reynolds number. The conservative variable vector $\mathbf{Q}$, the inviscid flux vector $\mathbf{E}$, and the viscous flux vector $\mathbf{R}$ are expressed as follows and the rest can be expressed following the symmetric rule:

$$\mathbf{Q}=\begin{pmatrix}\bar{\rho}\\ \bar{\rho}\tilde{u}\\ \bar{\rho}\tilde{v}\\ \bar{\rho}\tilde{w}\\ \bar{\rho}\tilde{e}\end{pmatrix} \tag{5}$$

$$\mathbf{E}=\begin{pmatrix}\bar{\rho}\tilde{u}\\ \bar{\rho}\tilde{u}^2+\bar{p}\\ \bar{\rho}\tilde{u}\tilde{v}\\ \bar{\rho}\tilde{u}\tilde{w}\\ (\bar{\rho}\tilde{e}+\bar{p})\tilde{u}\end{pmatrix} \tag{6}$$

$$\mathbf{R}=\begin{pmatrix}0\\ \bar{\tau}_{xx}+\sigma_{xx}\\ \bar{\tau}_{xy}+\sigma_{xy}\\ \bar{\tau}_{xz}+\sigma_{xz}\\ Q_x\end{pmatrix} \tag{7}$$

The overbar denotes a regular-filtered variable as given in Eq. (1), and the tilde is used to denote the Favre-filtered variable defined in Eq. (2). In the above equations, ρ is the density, u, v, w are the Cartesian velocity components in the x, y, z directions, p is the static pressure, and e is the total energy per unit mass.

The $\bar{\tau}$ is the molecular viscous stress tensor and is estimated as

$$\bar{\tau}_{ij}=\frac{2}{3}\tilde{\mu}\frac{\partial \tilde{u}_k}{\partial x_k}\delta_{ij}+\tilde{\mu}\left(\frac{\partial \tilde{u}_i}{\partial x_j}+\frac{\partial \tilde{u}_j}{\partial x_i}\right),\quad i,j=1,2,3 \tag{8}$$

The above equation is in the tensor form, where the subscripts 1, 2, 3 represent the coordinates, x, y, z and the Einstein summation convention is used. The molecular viscosity $\tilde{\mu}=\tilde{\mu}(\tilde{T})$ is determined by Sutherland law.

The σ is the subgrid-scale (SGS) stress tensor due to the filtering process and is expressed as

$$\sigma_{ij}=-\bar{\rho}(\widetilde{u_i u_j}-\tilde{u}_i\tilde{u}_j) \tag{9}$$

The energy flux Q is expressed as

$$Q_i=\tilde{u}_j(\bar{\tau}_{ij}+\sigma_{ij})-\bar{q}_i+\Phi_i \tag{10}$$

where Φ is the subscale heat flux:

$$\Phi_i=-C_p\bar{\rho}(\widetilde{u_i T}-\tilde{u}_i\tilde{T}) \tag{11}$$

The $\bar{q}_i$ is the molecular heat flux:

$$\bar{q}_i=-\frac{\tilde{\mu}}{(\gamma-1)Pr}\frac{\partial a^2}{\partial x_i} \tag{12}$$

where $a=\sqrt{\gamma R\tilde{T}}$ is the speed of sound. The equation of state as a constitutive equation relating density to pressure and temperature is defined as

$$\bar{\rho}\tilde{e}=\frac{\bar{p}}{(\gamma-1)}+\frac{1}{2}\bar{\rho}(\tilde{u}^2+\tilde{v}^2+\tilde{w}^2)+\rho k \tag{13}$$

where γ is the ratio of specific heats, ρk is the subscale kinetic energy per unit volume.

$$\rho k=\frac{1}{2}\bar{\rho}(\widetilde{u_i u_i}-\tilde{u}_i\tilde{u}_i)=-\frac{1}{2}\sigma_{ii} \tag{14}$$

The closure of Eq. (4) requires a model for the subgrid-scale stress σ_{ij} and heat flux Φ_i. Most subgrid-scale models employ the eddy viscosity($\tilde{\mu}_t$) approach to avoid solving additional equations. In this study, the standard Smagorinsky model with Van Driest damping [18] is used to model the subgrid-scale stress. With the Smagorinsky model, the eddy viscosity is written as

$$\tilde{\mu}_t=\bar{\rho}C_s^2 l^2\sqrt{2S_{ij}S_{ij}} \tag{15}$$

where C_s is the Smagorinsky constant, and l is the model length scale. In this study, the value 0.2 was used for C_s, and

$$l=(\Delta)^{1/3}\sqrt{(1-\exp(-y^+/26))^3} \tag{16}$$

where Δ is the volume of the cell. S_{ij} is the rate-of-strain tensor.

In generalized coordinates(ξ, η, ζ), the governing Eq. (4) can be expressed as the following conservative form:

$$\frac{\partial Q}{\partial t}+\frac{\partial E}{\partial \xi}+\frac{\partial F}{\partial \eta}+\frac{\partial G}{\partial \zeta}=\frac{1}{\mathrm{Re}}\left(\frac{\partial R}{\partial \xi}+\frac{\partial S}{\partial \eta}+\frac{\partial T}{\partial \zeta}\right) \tag{17}$$

The conservative variable vector Q, the inviscid flux vectors E, F, G, and the viscous fluxes R, S, T are expressed as

$$Q=\frac{1}{J}\begin{pmatrix}\bar{\rho}\\ \bar{\rho}\tilde{u}\\ \bar{\rho}\tilde{v}\\ \bar{\rho}\tilde{w}\\ \bar{\rho}\tilde{e}\end{pmatrix} \tag{18}$$

$$E=\begin{pmatrix}\bar{\rho}U\\ \bar{\rho}\tilde{u}U+l_x\bar{p}\\ \bar{\rho}\tilde{v}U+l_y\bar{p}\\ \bar{\rho}\tilde{w}U+l_z\bar{p}\end{pmatrix} \tag{19}$$

$$F=\begin{pmatrix}\bar{\rho}V\\ \bar{\rho}\tilde{u}V+m_x\bar{p}\\ \bar{\rho}\tilde{v}V+m_y\bar{p}\\ \bar{\rho}\tilde{w}V+m_z\bar{p}\end{pmatrix} \tag{20}$$

$$G=\begin{pmatrix}\bar{\rho}W\\ \bar{\rho}\tilde{u}W+n_x\bar{p}\\ \bar{\rho}\tilde{v}W+n_y\bar{p}\\ \bar{\rho}\tilde{w}W+n_z\bar{p}\end{pmatrix} \tag{21}$$

$$R=\begin{pmatrix}0\\ l_k\bar{\tau}_{xk}\\ l_k\bar{\tau}_{yk}\\ l_k\bar{\tau}_{zk}\\ l_k(\tilde{u}_i\bar{\tau}_{ki}-\bar{q}_k)\end{pmatrix} \tag{22}$$

$$S=\begin{pmatrix}0\\ m_k\bar{\tau}u_{xk}\\ m_k\bar{\tau}_{yk}\\ m_k\bar{\tau}u_{zk}\\ m_k(\tilde{u}_i\bar{\tau}_{ki}-\bar{q}_k)\end{pmatrix} \tag{23}$$

$$T=\begin{pmatrix}0\\ n_k\bar{\tau}_{xk}\\ n_k\bar{\tau}_{yk}\\ n_k\bar{\tau}_{zk}\\ n_k(\tilde{u}_i\bar{\tau}_{ki}-\bar{q}_k)\end{pmatrix} \tag{24}$$

where U, V, and W are the contravariant velocities in ξ, η, ζ directions and are defined as follows:

$$U = l_t + \mathbf{l} \bullet \mathbf{V} = l_t + l_x\tilde{u} + l_y\tilde{v} + l_z\tilde{w} \tag{25}$$

$$V = m_t + \mathbf{m} \bullet \mathbf{V} = m_t + m_x\tilde{u} + m_y\tilde{v} + m_z\tilde{w} \tag{26}$$

$$W = n_t + \mathbf{n} \bullet \mathbf{V} = n_t + n_x\tilde{u} + n_y\tilde{v} + n_z\tilde{w} \tag{27}$$

where l_t, m_t, and n_t are the components of the interface contravariant velocity of the control volume in ξ, η, and ζ directions, respectively. $\mathbf{l}$, $\mathbf{m}$, and $\mathbf{n}$ denote the normal vectors located at the centers of ξ, η, and ζ interfaces of the control volume with their magnitudes equal to the surface areas and pointing to the directions of ξ, η, and ζ gradient. J is the Jacobian of the transformation.

3 Implicit Time Integration

The time dependent governing equation (17) is solved using the dual time stepping method suggested by Jameson [19]. A pseudo temporal term $\partial Q/\partial\tau$ is added to the governing Eq. (17). This term vanishes at the end of each physical time step and has no influence on the accuracy of the solution. An implicit pseudo time marching scheme using line Gauss–Seidel relaxation is employed to achieve high convergence rate instead of using the explicit scheme as given by Jameson [19]. The physical temporal term is discretized implicitly using a three point second-order accuracy, backward differencing as the following:

$$\frac{\partial \mathbf{Q}}{\partial t} = \frac{3\mathbf{Q}^{\mathbf{n+1}} - 4\mathbf{Q}^{\mathbf{n}} + \mathbf{Q}^{\mathbf{n-1}}}{2\Delta t} \tag{28}$$

where $n-1$, n, and $n+1$ are three sequential time levels, which have a time interval of Δt. The first-order Euler scheme is used to discretize the pseudo temporal term. The semidiscretized equations of the governing equations are finally given as the following:

$$\left[\left(\frac{1}{\Delta\tau} + \frac{1.5}{\Delta t}\right)I - \left(\frac{\partial R}{\partial \mathbf{Q}}\right)^{n+1,m}\right]\delta\mathbf{Q}^{\mathbf{n+1,m+1}} = R^{n+1,m} - \frac{3\mathbf{Q}^{\mathbf{n+1,m}} - 4\mathbf{Q}^{\mathbf{n}} + \mathbf{Q}^{\mathbf{n-1}}}{2\Delta t} \tag{29}$$

where $\Delta\tau$ is the pseudo time step, and R is the net flux discretized in space. The low diffusion E-CUSP (LDE) scheme [13,20] is used to evaluate the inviscid flux with the fifth-order WENO scheme [14] and the fourth-order central differencing is used for the viscous flux [15].

4 Boundary Conditions

The Reynolds number based on freestream velocity and chord length is 1.19179×10^5. The freestream Mach number tested in the experiment is 0.03, but the Mach number used in the computation is 0.05. The reason is to avoid the convergence stiffness. The experiment indicates that all the nondimensional performance coefficients including lift and drag are insensitive to the Mach number in the tested low Mach number range. Steady-state freestream conditions are used for the upstream portion of the farfield boundary. For the downstream farfield boundary, the static pressure was specified as freestream value, and the streamwise gradients of other variables were forced to vanish. The periodic boundary condition is used in a spanwise direction. The wall treatment suggested in Refs. [14,15] to achieve the flux conservation by shifting a half interval of the mesh on the wall is employed. The no slip condition is employed on the airfoil surface. For computing the flux $F_{1/2}$ on the wall, there is

$$G_w = \begin{pmatrix} \rho V \\ \rho uV + p\eta_x \\ \rho vV + p\eta_y \\ \rho wV + p\eta_z \\ (\rho e + p)V \end{pmatrix}_w = \begin{pmatrix} 0 \\ p\eta_x \\ p\eta_y \\ p\eta_z \\ 0 \end{pmatrix}_w \tag{30}$$

and a third-order accuracy wall boundary formula is used to evaluate $p|_w$:

$$p_w = \frac{1}{6}(11p_1 - 7p_2 + 2p_3) \tag{31}$$

At the injection cavity, total pressure and total temperature are specified and the flow angle is normal to the inlet surface, whereas the static pressure is given at the suction cavity. To achieve zero net mass flux with the CFJ flow control, the mass flow that exits the injection slot must be equal to the mass flow entering the suction slot. This is achieved by adjusting the total pressure in the injection cavity and the static pressure in the suction cavity. The process is iterated throughout the simulation until the difference between the injection and suction mass flow rates is within the desired value.

$$\left|\frac{\dot{m}_{j1} - \dot{m}_{j2}}{\dot{m}_{j1}}\right| < \varepsilon \tag{32}$$

where $\dot{m}_{j1}$ represents the injection mass flow, $\dot{m}_{j2}$ denotes the injection mass flow, and ε is 0.02 in this LES simulation as the mass flow convergence criterion.

5 LES Mesh

The CFJ airfoil modified from the NACA6415 airfoil and tested by Dano et al. [12] is shown in Fig. 1. The chord length (C) of the airfoil is 0.3048 m and the design span is 0.5906. The computation mesh is constructed using the O-mesh topology in order to improve the mesh quality around airfoil. Figures 2 and 3 show the LES mesh for CFJ at a 30 deg AOA. The farfield boundary locates 75 times chord from the CFJ center chord. The spanwise length used is 15%C.

LES is very central processing unit intensive, in particular for CFJ airfoil, which needs to iterate the suction slot static pressure to match the injection mass flow. We, hence, designed the mesh based on the previous successful experience of other researchers and our own LES cases. Mary and Sagaut [21] simulated the flows over an airfoil near stall at a chord Reynolds number of 2.1×10^6 using several mesh sizes. Their coarse mesh has the surface mesh resolution of $\Delta x^+ \approx 800$, $\Delta y^+ \approx 2$, $\Delta z^+ \approx 200$. Their finest mesh with the size of roughly 7×10^6 cells has the surface resolution of $\Delta x^+ \approx 100$, $\Delta y^+ \approx 2$, $\Delta z^+ \approx 20$. Their computed mean and fluctuating velocity profiles compare reasonably well with experimental measurements. The wing span chosen by most LES studies [21–24] are less than 5%C length. Mary and Sagaut [21] studied three different span lengths of 0.5%C, 1.2%C, and 3%C and found little effect on the flow properties near/post stall.

The mesh resolution we adopted for this research is similar to the fine mesh of Mary and Sagaut [21] and is approximately within the guideline of LES mesh requirement suggested by Chapman [25]. The mesh points of 451 are placed around airfoil with 301

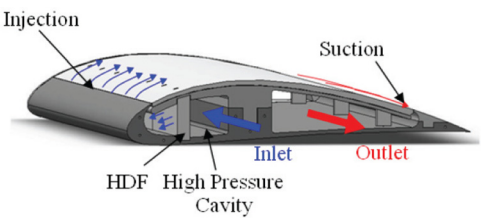

Fig. 1 CFJ airfoil concept

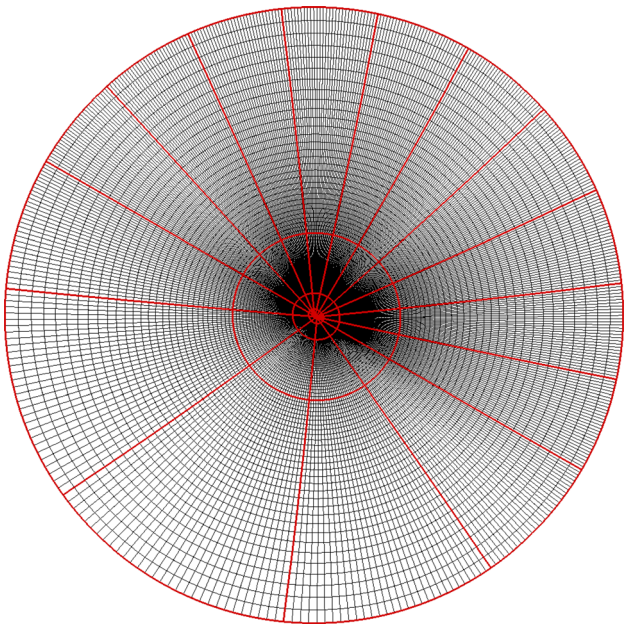

Fig. 2 LES mesh for the CFJ airfoil at 30 deg AOA, total mesh = 7,913,835, *h*(span) = 0.15 *C*(chord)

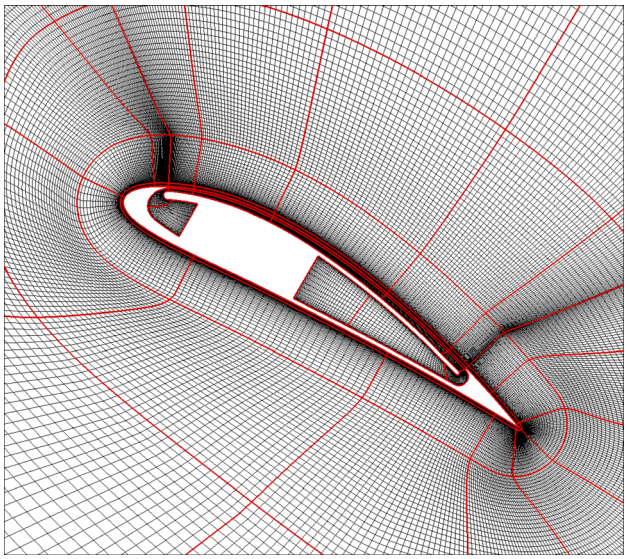

Fig. 3 LES mesh around the CFJ airfoil at 30 deg AOA

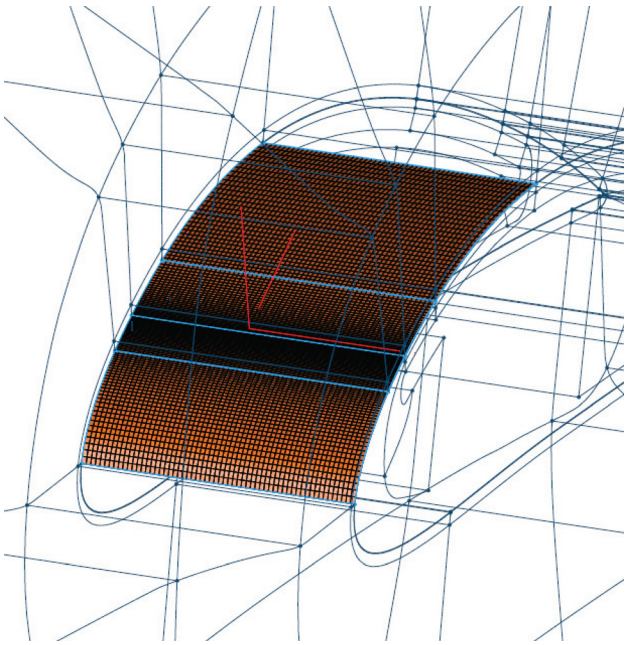

Fig. 4 LES mesh on the suction surface of the CFJ airfoil

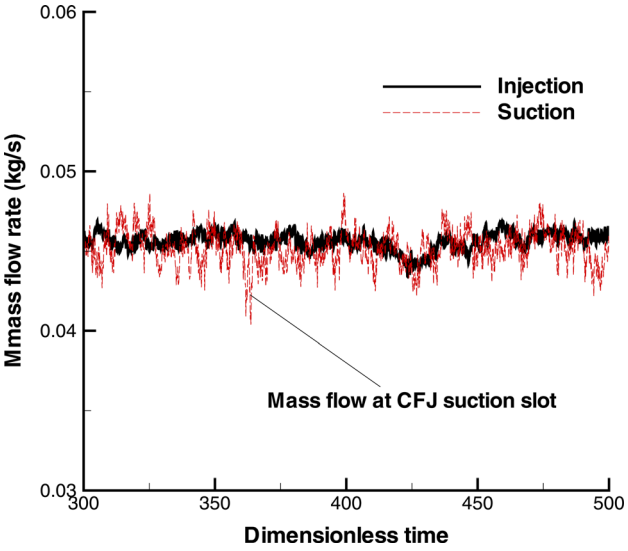

Fig. 5 Mass flow rate at injection and suction slot of the CFJ airfoil predicted by LES at AOA of 25 deg for $C_\mu = 0.15$, $R_e = 1.19179 \times 10^5$, $M = 0.05$

points on the suction surface and 151 points on the pressure surface. A total of 211 points is used normal to the airfoil surface and 61 points are distributed in the spanwise direction. The total mesh size is 7.913835×10^6 and is partitioned to 135 blocks for the parallel computation. With the Reynolds number of 1.19179×10^5, the mesh has the y^+ about unity for the first grid point normal to the wall, and Δx^+ and Δz^+ are about 40 on the CFJ airfoil surface with almost equal size over the CFJ airfoil, as presented in Fig. 4. The same mesh resolution is studied with mesh refinement in the previous LES computation of our group by Shen and Zha [26] and yields good results. The mesh size utilized in this study is, thus, considered as adequate for the LES of CFJ airfoil.

6 Jet Momentum Coefficient C_μ

For CFJ airfoil, C_μ is used as an important parameter for jet mass flow control. The jet momentum coefficient, a dimensionless parameter that includes mass flow rate and jet velocity, is defined as

$$C_\mu = \frac{\dot{m}_j V_j}{\frac{1}{2}\rho_\infty V_\infty^2 S} \tag{33}$$

where $\dot{m}_j$ is CFJ injection mass flow rate, V_j represents the injection jet velocity, the subscript $_\infty$ denotes freestream of the CFJ airfoil, and S is the airfoil planform area. In this paper two different momentum coefficients, $C_\mu = 0.008$ and $C_\mu = 0.15$, are studied. It usually needs a few iterations to adjust the mass flow difference between injection and suction to be less than 2%. Figure 5 shows the time history of the mass flow at injection and suction at an AOA of 25 deg for $C_\mu = 0.15$ predicted by the LES. The mass flow at suction shows a larger fluctuation than the injection since the flow near the suction slot is highly unstable due to the mixing of the attached coflow jet with freestream shear flow.

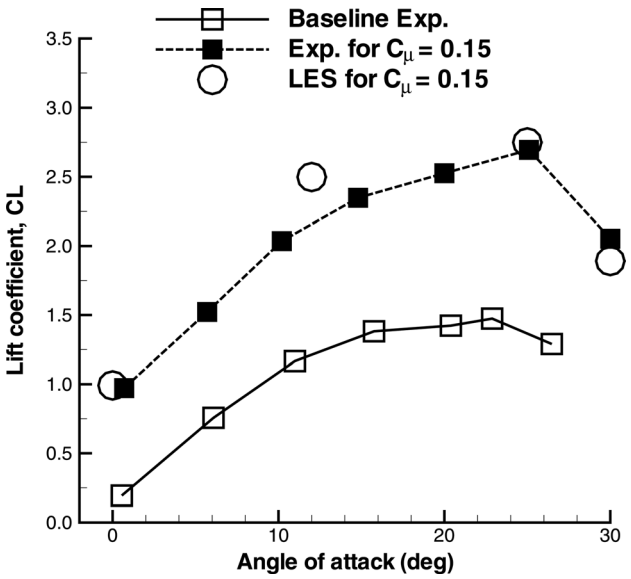

Fig. 6 Predicted lift(C_L) coefficients of the CFJ airfoil at AOA of 0 deg, 12 deg, 25 deg, 30 deg; $R_e = 1.19179\times10^5$, $M = 0.05$

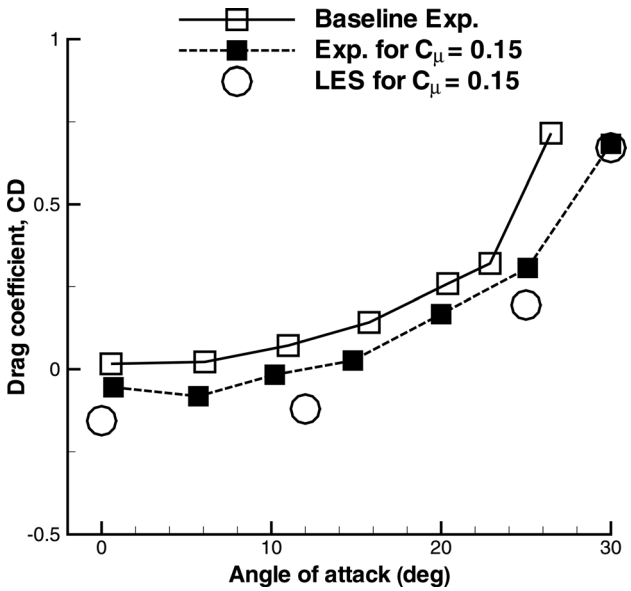

Fig. 7 Predicted drag(C_D) coefficients of the CFJ airfoil at AOA of 0 deg, 12 deg, 25 deg, 30 deg; $R_e = 1.19179\times10^5$, $M = 0.05$

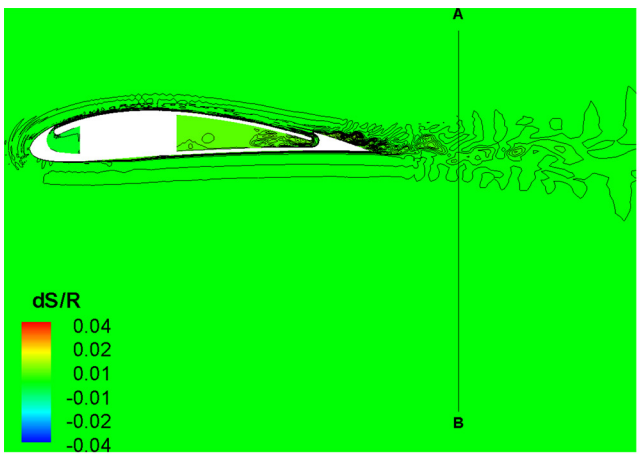

(a)

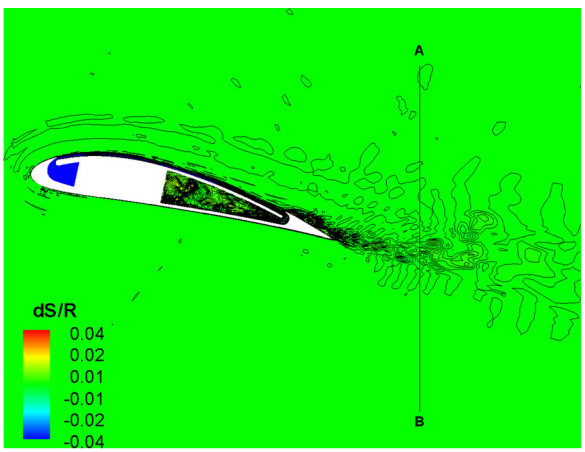

(b)

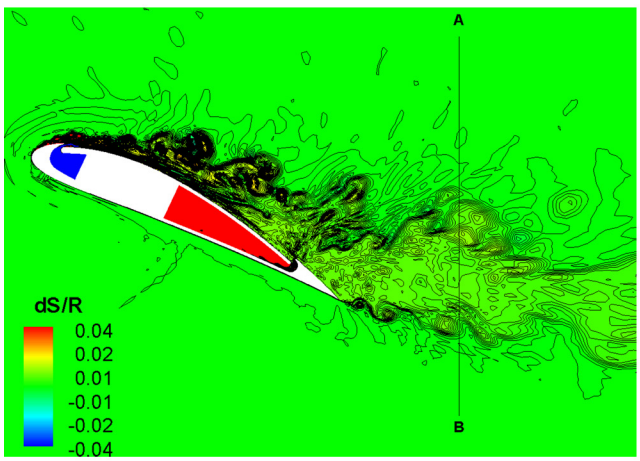

(c)

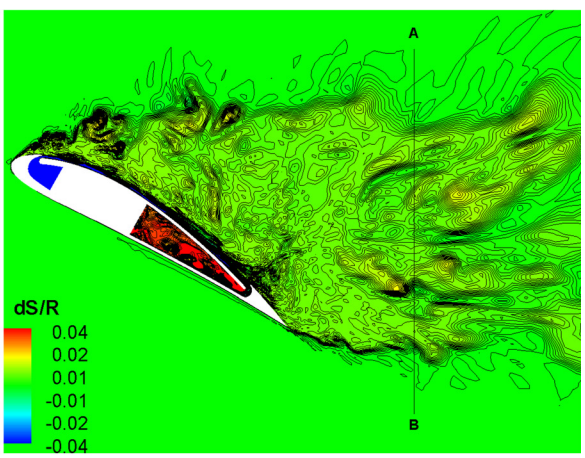

(d)

Fig. 8 Instantaneous entropy ($\Delta S/R = \gamma/1-\gamma \ln Tt/Tt_\infty - \ln Pt/Pt_\infty$) of the CFJ airfoil for $C_\mu = 0.15$ at AOA of 0 deg, 12 deg, 25 deg, 30 deg; $R_e = 1.19179\times10^5$, $M = 0.05$

7 Lift and Drag Calculation

The momentum and pressure at the injection and suction slots produce a reactionary force, which is automatically measured by the force balance in wind tunnel testing. However, for CFD simulation, the full reactionary force is difficult to obtain unless the complete internal ducts of injection and suction are simulated. Using control volume analysis, the reactionary force can be calculated using the flow parameters at the injection and suction slot opening surfaces [2]. Zha et al. [2] give the following formulations to calculate the lift and drag due to the jet reactionary force for a CFD simulation. By considering the effects of injection and suction jets on the CFJ airfoil, the expressions for these reactionary forces are given as [2]

$$F_{y_{cfj}} = (\dot{m}_{j1}V_{j1} + p_{j1}A_{j1}) * \sin(\theta_1 - \alpha) + \gamma(\dot{m}_{j2}V_{j2} + p_{j2}A_{j2}) * \sin(\theta_2 + \alpha) \quad (34)$$

$$F_{y_{cfj}} = (\dot{m}_{j1}V_{j1} + p_{j1}A_{j1}) * \sin(\theta_1 - \alpha) + \gamma(\dot{m}_{j2}V_{j2} + p_{j2}A_{j2}) * \sin(\theta_2 + \alpha) \quad (35)$$

where the subscripts 1 and 2 stand for the injection and suction, respectively, and θ_1 and θ_2 are the angles between the injection and suction slot's surface and a line normal to the airfoil chord. α is the angle of attack. γ denotes the suction coefficient; if no suction, γ equals 0.

The total lift and drag on the airfoil can then be expressed as

$$D = R'_x - F_{x_{cfj}} \quad (36)$$

$$L = R'_y - F_{y_{cfj}} \quad (37)$$

where R'_x and R'_y are the surface integral of pressure and shear stress in x (drag) and y (lift) direction, excluding the internal ducts of injection and suction. For the CFD simulation, the total lift and drag are calculated using Eqs. (36) and (37).

8 Results and Discussion

In this study, LES of the CFJ is first conducted at various angles of attack including 0 deg, 12 deg, 25 deg, and 30 deg for $C_\mu = 0.15$ in order to compare with the measured lumped parameters such as the coefficients of lift and drag obtained in Ref. [12]. Under these conditions, the flows are massively separated at an AOA of 30 deg. The mass flow between the injection and the suction cavity is balanced within 2%. For the unsteady LES

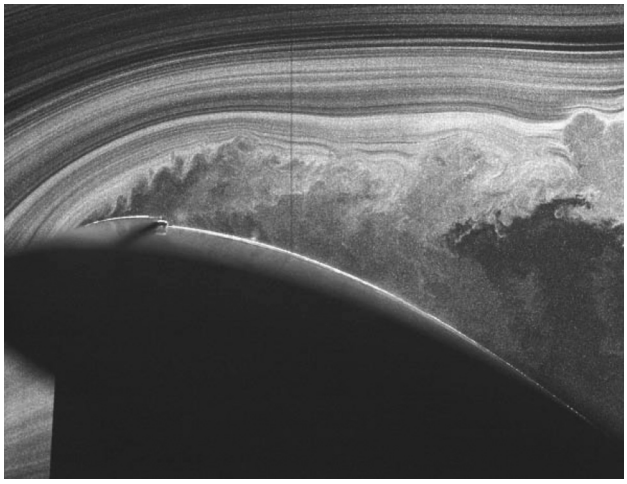

Fig. 9 Instantaneous smoke visualization of the CFJ airfoil by experiment; AOA = 30 deg, $C_\mu = 0.15$ (bottom), $R_e = 1.19179 \times 10^5$, $M = 0.05$

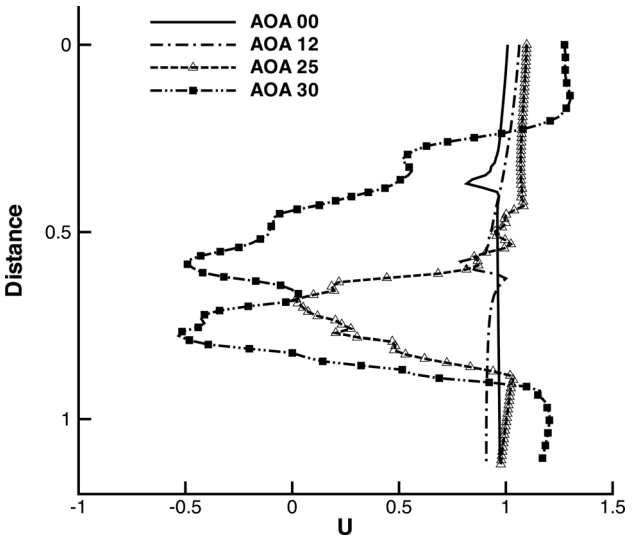

Fig. 10 Instantaneous axial velocity (U) at axial plane $\overline{AB}$ of the CFJ airfoil for $C_\mu = 0.15$, $R_e = 1.19179 \times 10^5$, $M = 0.05$

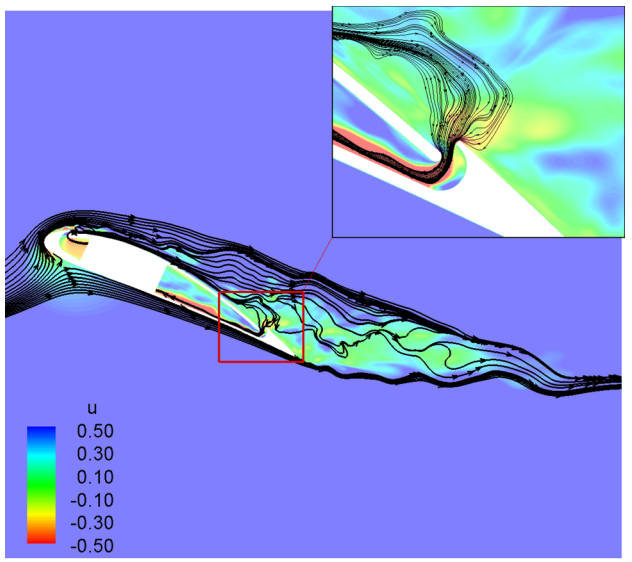

(a)

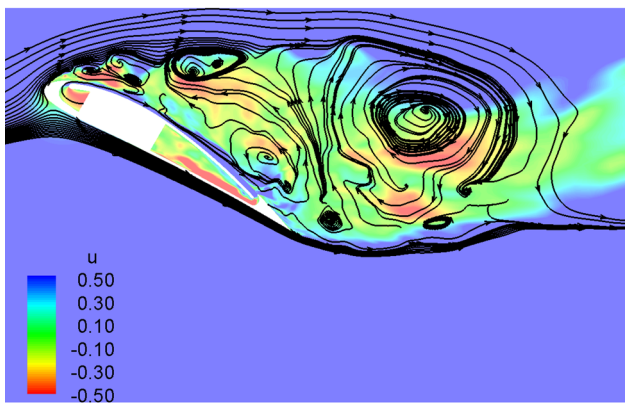

(b)

Fig. 11 Instantaneous CFJ stalled flows contoured by axial velocity (U) for $C_\mu = 0.15$, $R_e = 1.19179 \times 10^5$, $M = 0.05$; AOA = 25 deg (top), AOA = 30 deg (bottom)

simulation, a nondimensional time step of about 0.025 is used. The unsteady simulations start from the initial flow field using a few thousand steps of steady-state calculation. The residual is typically reduced by three orders of magnitude in each physical time step. All the LES results presented in this paper are plotted at the center span plane (0.075 h).

The time averaged lift and drag coefficient predicted by the LES is plotted with the experimental results from Ref. [12] in Figs. 6 and 7 for $C_\mu = 0.15$. The LES underpredicts the lift and drag coefficient at an AOA of 30 deg by 7.8% and 1.7%, respectively. This is a remarkable improvement compared to the detached eddy simulation (DES) prediction of a separated CFJ airfoil flow with lift and drag underpredicted by 22% and 64% at the high angle of attack [7], e.g., unsteady Reynolds averaged Navier-Stokes (URANS)/DES simulations [7] are conducted using a typical O-mesh of total mesh size of 817,152 cells and using the same numerical schemes employed in this LES simulation. The lift and drag measurement uncertainty is about 1% [6]. The overall lift and drag agree reasonably well with the experiment as shown in Figs. 6 and 7, with the lift slightly overpredicted and the drag underpredicted when the AOA is less than 30 deg. An advantage of CFJ flow control airfoil is the increased stall margin. Both the LES and experiment indicate that the CFJ for $C_\mu = 0.15$ stalls around an AOA of 25 deg, whereas the stall angle of the baseline CFJ airfoil without the coflow jet is around an AOA of 23 deg [5,6,27].

Figure 8 shows instant entropy $((\Delta S/R) = (\gamma/(1-\gamma))\ln(Tt/Tt_\infty) - \ln(Pt/Pt_\infty))$ of the CFJ airfoil for $C_\mu = 0.15$ at AOAs of 0 deg, 12 deg, 25 deg, and 30 deg, where Pt_∞ and Tt_∞ denote normalized freestream total pressure and total temperature. R is the universal gas constant and γ is the specific heat ratio of air taken the value of 1.4. Note that negative entropy is due to the added energy by the coflow jet at the injection slot. Entropy can represent the flow energy loss due to flow separation and trailing edge wake. For the AOA of 0 deg and 12 deg, the significant entropy increase is mostly at the wake region since the attached boundary layer does not generate as much energy loss as the wake. For AOAs 25 deg and 30 deg, the flow is separated near the CFJ leading edge and the entropy increase occurs at most of the area behind the airfoil. The LES captures clearly vortex shedding originated from the leading edge separation.

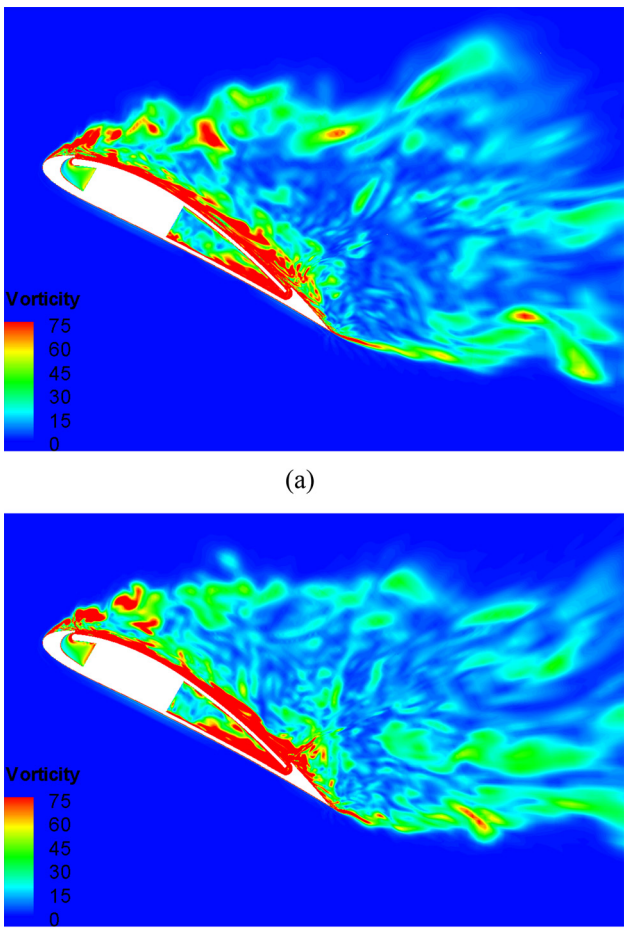

Fig. 12 Instantaneous vorticity near the injection slot of the CFJ airfoil at AOA = 30 deg predicted by LES; $C_\mu = 0.08$ (top), $C_\mu = 0.15$ (bottom), $R_e = 1.19179\times10^5$, $M = 0.05$

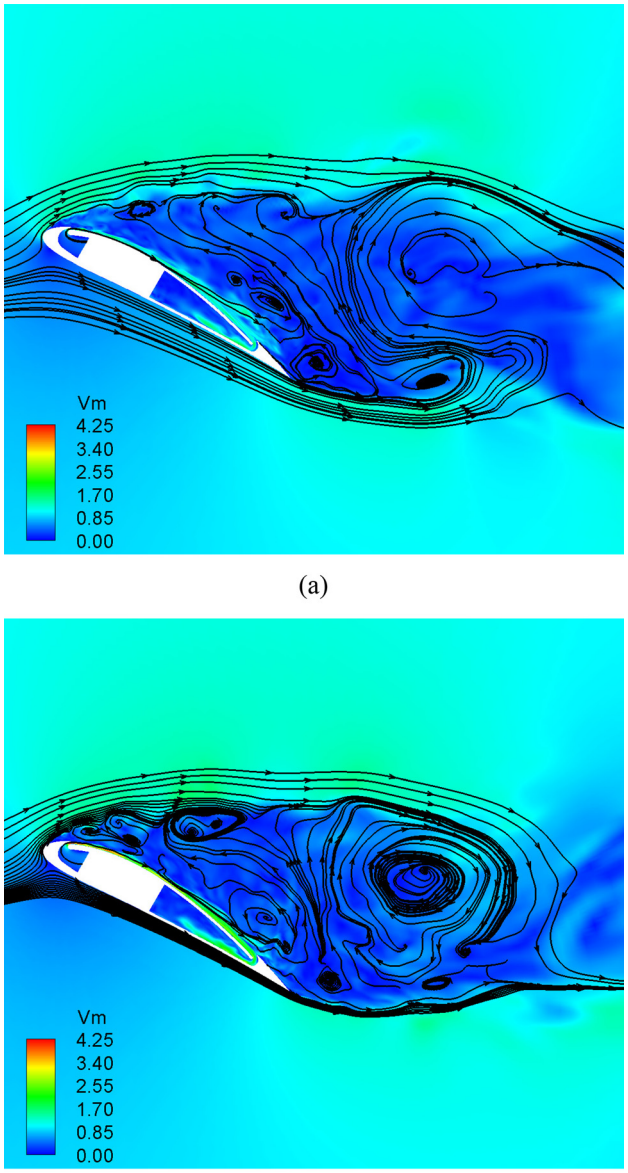

Fig. 13 Instantaneous CFJ stalled flows contoured by velocity magnitude (*Vm*) for $C_{mu} = 0.08$ (top), $C_{mu} = 0.15$ (bottom); AOA = 30 deg, $R_e = 1.19179\times10^5$, $M = 0.05$

The simulated massive separation flow structure at an AOA of 30 deg in Fig. 8 is in good qualitative agreement with the experimental flow visualization as shown in Fig. 9 [12]. The vortex shedding due to the flow separation from the CFJ airfoil leading edge is well captured by the present LES.

Figure 10 is the instantaneous velocity profiles in the wake along plane $\overline{AB}$, which is located at 1/4 quarter chord downstream

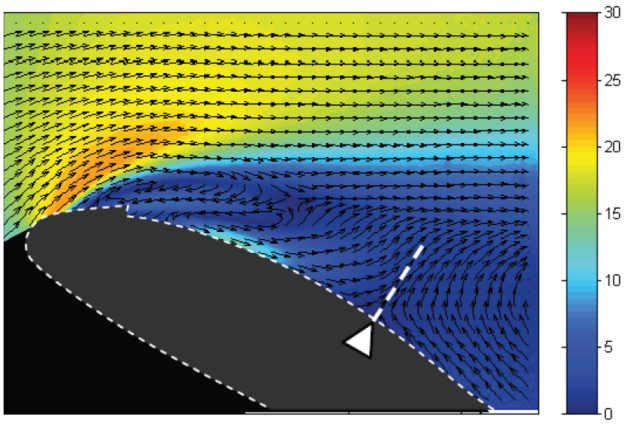

Fig. 14 Time average velocity (m/s) field of the CFJ airfoil at AOA = 30 deg for $C_\mu = 0.15$ by the experiment; $R_e = 1.19179 \times 10^5$, $M = 0.05$

of the trailing edge and has the length of about 1.1 times of the chord length. The y-axis represents the distance from point A to B. The axial velocity has a very shallow deficit due to CFJ energized main flow near the trailing edge when the flow is attached at AOA = 0 deg 0 and 12 deg. For AOAs of 25 deg and 30 deg, the velocity deficit is enormous due to the massive flow separation. The wake width is about 10% of $\overline{AB}$ for AOA 0 deg, 17% for AOA 12 deg, 25% for AOA 25 deg, and 60% for AOA 30 deg.

The negative velocity takes roughly 35% of $\overline{AB}$ for AOA 30 deg due to the massive recirculation, as illustrated in Fig. 11 (bottom). The CFJ is not able to be maintained as a continuous jet from injection to suction due to the low momentum of the massively separated flow induced by the very severe adverse pressure gradient. For an angle of attack of 25 deg, no negative axial velocity, or no reversed flow, is generated at that instant since the CFJ is barely maintained as a continuous jet and is able to transfer energy to the main flow more effectively than an AOA of 30 deg.

For comparison of different jet strength effects on highly separated flow, vorticity contours for $C_\mu = 0.08$ (top) and $C_\mu = 0.15$ (bottom) are displayed in Fig. 12. Figure 12 indicates that the LES captures many small-scale structures of the separated flow. With the stronger jet of $C_\mu = 0.15$, the wake mixing width is smaller.

Figure 13 shows instantaneous velocity contours of the CFJ. The recirculation area or wake width near the trailing edge plane for $C_\mu = 0.08$ is larger than that of $C_\mu = 0.15$.

Figure 14 shows the measured time average velocity field of the CFJ airfoil colored by velocity magnitude for $C_\mu = 0.15$ at 30 deg AOA. In the experiment, 1000 instantaneous velocity fields samples were acquired by using the particle image velocimetry (PIV) [12]. The white triangle marks the saddle point where the recirculating flow from the trailing edge merges with the recirculating flow from the leading edge and generates a stream normal to the airfoil surface.

The computed instantaneous flow field of the CFJ airfoil colored by velocity magnitude for $C_\mu = 0.15$ is shown in Fig. 15. The saddle point has about the same location as that measured in the experiment. The LES reveals that the outer shear layer is sucked into and mixed with the attached coflow jet near the wall surface.

Figure 16 compares the instantaneous streamlines in the shear layer mixing region with the attached coflow jet at the bottom wall surface. Compared with the case of $C_\mu = 0.08$, the flow with $C_\mu = 0.15$ withdraws more flow into the suction cavity with stronger mixing as expected.

Figure 17 demonstrates the computed streamwise (top), shear (middle), and lateral (bottom) Reynolds stress at 0.25, and 1 chord downstream for $C_\mu = 0.15$ and $C_\mu = 0.08$, respectively. At 0.25 chord downstream, the streamwise and shear Reynolds stress are almost the same for $C_\mu = 0.15$ and $C_\mu = 0.08$, but the lateral Reynolds stress ($v'v'$) for $C_\mu = 0.15$ is a little larger than at one chord downstream of the trailing edge; all the Reynolds stresses are greater than those at upstream 0.25 chord location. It indicates that the turbulence fluctuation is enhanced up to one chord location due to the large vortex shedding. The stronger jet with $C_\mu = 0.15$ has greater Reynolds stress terms, indicating a stronger

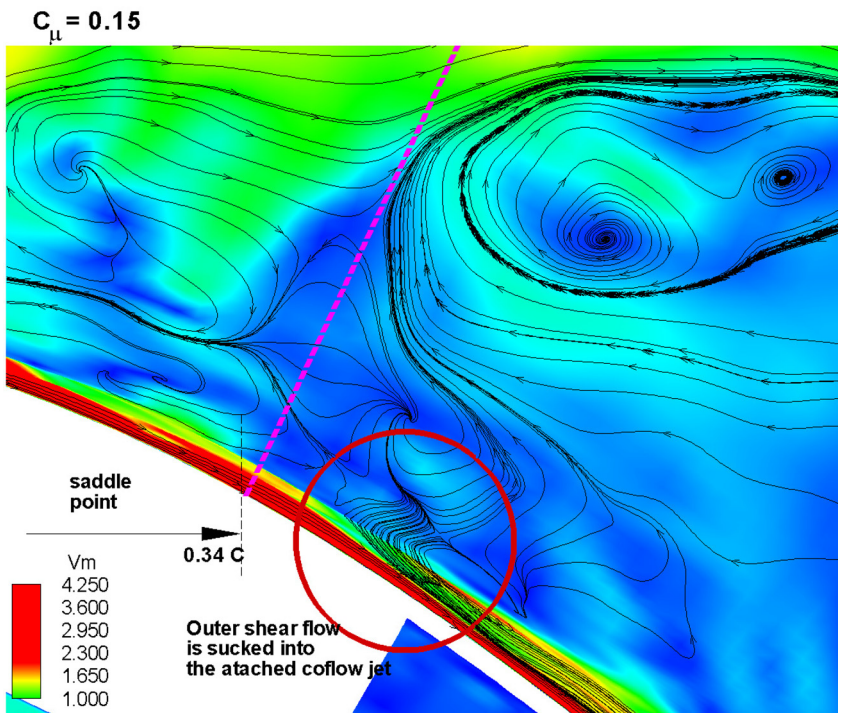

Fig. 15 Contours of velocity magnitude and streamlines of the CFJ airfoil for $C_\mu = 0.15$, $R_e = 1.19179 \times 10^5$, $M = 0.05$ predicted by LES; AOA = 30 deg, time averaged(top), instantaneous(bottom)

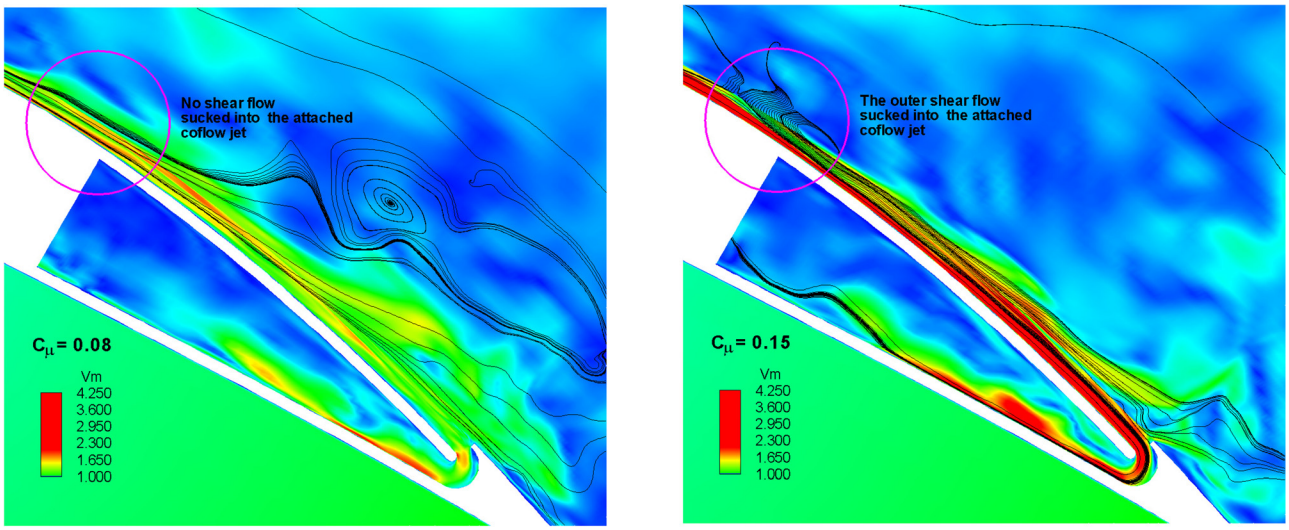

(a) (b)

Fig. 16 Instantaneous streamlines indicating mixing of the outer shear flow with the attached coflow jet predicted by LES; AOA = 30 deg, $C_{mu} = 0.08$ (top), $C_{mu} = 0.15$ (bottom), $R_e = 1.19179 \times 10^5$, $M = 0.05$

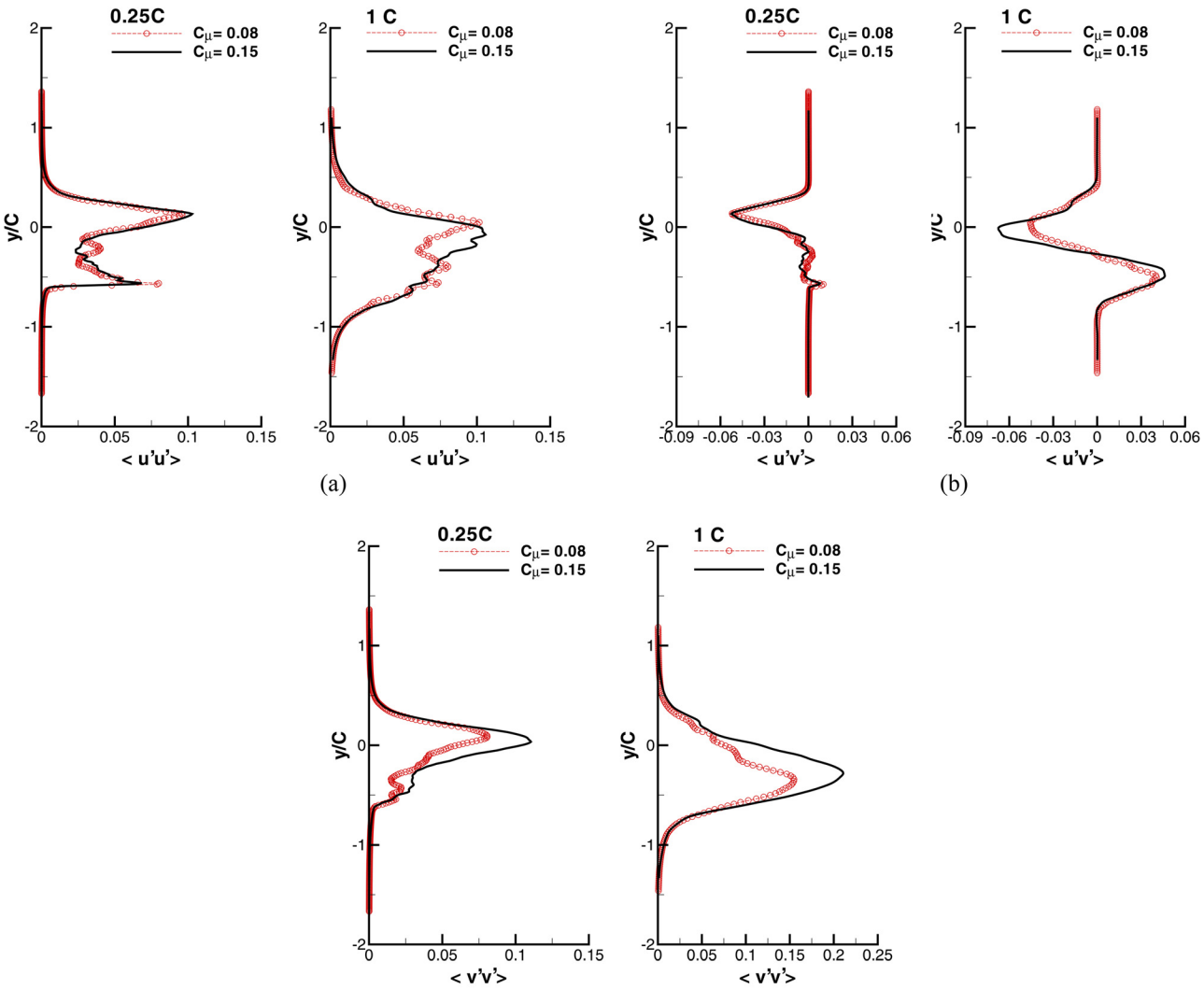

Fig. 17 Reynolds stress of the CFJ airfoil at 30 deg AOA, $R_e = 1.19179 \times 10^5$, $M = 0.05$ predicted by LES; streamwise (top), shear (middle), lateral (bottom)

mixing effect even though with a narrower wake width, as shown in Figs. 12 and 13.

9 Conclusions

The LES using high-order schemes achieves a reasonably good prediction of lift and drag of the CFJ at various angles of attack of 0 deg, 12 deg, 25 deg, and 30 deg. The flow structures under a large massive flow separation of the CFJ airfoil at 30 deg AOA is investigated for jet momentum coefficients of $C_\mu = 0.15$ and 0.08. The LES predicts the large vortex structures in good agreement with the experimental observation. The saddle point that merges the large recirculating flow from the trailing edge with the one from the leading edge is well resolved. The stronger jet of $C_\mu = 0.15$ has a narrower wake but high Reynolds stresses, indicating a more enhanced mixing effect. The Reynolds stress terms are also greater at one chord downstream location than at 1/4 chord location, showing that the turbulence intensity is increased instead of decaying due to the large vortex shedding up to one chord distance downstream of the airfoil trailing edge. Overall, the LES significantly improves the quantitative prediction of the lift and drag compared with the previous URANS and DES for CFJ flow at high AOA and the vortex structures of separated flows agree qualitatively with the experiment.

Acknowledgment

This research is supported under ARO/AFOSR Grant 50827-RT-1SP.

Nomenclature

C_μ = jet momentum coefficient, $\dot{m}_j V_j / \frac{1}{2}\rho_\infty V_\infty^2 S$
$\dot{m}_j$ = CFJ injection mass flow rate
M = Mach number
R_e = Reynolds number
V_j = CFJ injection jet velocity
V_∞ = air velocity at freestream of the CFJ airfoil
ρ_∞ = air density at freestream of the CFJ airfoil

References

[1] Zha, G.-C., Carroll, B., Paxton, C. D., Conley, A., and Wells, A., 2007, "High Performance Airfoil With Co-Flow Jet Flow Control," AIAA J., **45**, pp. 2087–2090.
[2] Zha, G.-C., Gao, W., and Paxton, C. D., 2007, "Jet Effects on Co-Flow Jet Airfoil Performance," AIAA J., **45**, pp. 1222–1231.
[3] Zha, G.-C., and Paxton, C. D., 2006, *A Novel Flow Control Method for Airfoil Performance Enhancement Using Co-Flow Jet*, "Applications of Circulation Control Technologies," AIAA, Reston, VA, Vol. 214, pp. 293–314.
[4] Zha, G.-C., Paxton, C. D., Conley, A., Wells, A., and Carroll, B., 2006, "Effect of Injection Slot Size on High Performance Co-Flow Jet Airfoil," AIAA J. Aircraft, **43**, pp. 987–995.
[5] Dano, B., Zha, G.-C., and Castillo, M., 2011, "Experimental Study of Co-Flow Jet Airfoil Performance Enhancement Using Discrete Jets," 49th AIAA Aerospace Sciences Meeting including the New Horizons Forum and Aerospace Exposition, Orlando, FL, Jan. 4–7, Paper No. AIAA-2011-941.
[6] Kirk, D., 2009, "Experimental and Numerical Investigations of a High Performance Co-Flow Jet Airfoil," Master thesis, Dept. of Mechanical and Aerospace Engineering, University of Miami, Miami, FL.
[7] Wang, B. Y., and Zha, G.-C., 2011, "Detached Eddy Simulation of a Co-Flow Jet Airfoil at High Angle of Attack," AIAA J. Aircraft, **48**, pp. 1495–1502.
[8] Orszag, S. A., 1970, "Analytical Theories of Turbulence," J. Fluid Mech., **41**, pp. 363–386.
[9] Mary, I., 2003, "Large Eddy Simulation of Vortex Breakdown Behind a Delta Wing," Int. J. Heat Fluid Flow, **24**, pp. 596–605.
[10] Eisenbach, S., and Friedrich, R., 2008, "Large Eddy Simulation of Flow Separation on an Airfoil at a High Angle of Attack and $Re = 10^5$ Using Cartesian Grids," Theor. Comput. Fluid Dyn., **22**, pp. 213–225.
[11] Moreau, S., Christopher, J., and Roger, M., 2008, "LES of the Trailing Edge Flow and Noise of a NACA0012 Airfoil Near Stall," Proceedings of the Summer Program 2008, Center for Turbulence Research.
[12] Dano, B., Kirk, D., and Zha, G.-C., 2010, "Experimental Investigation of Jet Mixing Mechanism of Co- Flow Jet Airfoil," 5th AIAA Flow Control Conference, Chicago, IL, June 28–July 1, Paper No. AIAA-2010-4421.
[13] Zha, G.-C., Shen, Y. Q., and Wang, B. Y., 2011, "An Improved Low Diffusion E-CUSP Upwind Scheme," J. Comput. Fluid., **48**, pp. 214–220.
[14] Shen, Y. Q., Zha, G.-C., and Wang, B. Y., 2009, "Improvement of Stability and Accuracy of Implicit WENO Scheme," AIAA J., **47**, pp. 331–334.
[15] Shen, Y. Q., Zha, G.-C., and Chen, X., 2009, "High Order Conservative Differencing for Viscous Terms and the Application to Vortex-Induced Vibration Flows," J. Comput. Phys., **228**(2), pp. 8283–8300.
[16] Wang, B. Y., and Zha, G.-C., 2008, "Detached Eddy Simulations of a Circular Cylinder Using a Low Diffusion E-CUSP and High-Order WENO Scheme," AIAA 38th Fluid Dynamics Conference, Seattle, WA, June 23–26, AIAA Paper No. 2008-3855.
[17] Knight, D., Zhou, D., Okong, N., and Shulka, V., 1998, "Compressible Large Eddy Simulation Using Unstructured Grids," AIAA Paper No. 98-0535.
[18] Smagorinsky, J. S., 1963, "General Circulation Experiments With the Primitive Equations, Part I: The Basic Experiments," Month. Weather Rev., **91**, pp. 99–152.
[19] Jameson, A., 1991. "Time Dependent Calculations Using Multigrid With Applications to Unsteady Flows Past Airfoils and Wings," AIAA Paper No. 91-1596.
[20] Zha, G.-C., Shen, Y. Q., and Wang, B. Y., 2008, "Calculation of Transonic Flows Using WENO Method With a Low Diffusion E-CUSP Upwind Scheme," 46th AIAA Aerospace Sciences Meeting, Reno, NV, Jan., AIAA Paper No. 2008-0745.
[21] Mary, I., and Sagaut, P., 2002, "Large Eddy Simulation of Flow Around an Airfoil Near Stall," AIAA J., **40**, pp.1139–1145.
[22] Mellen, C. P., Frohlich, J., and Rodi, W., 2003, "Lessons From LESFOIL Project on Large-Eddy Simulation of Flow Around an Airfoil," AIAA J., **41**, pp. 573–581.
[23] Dahlstrom, S., and Davidson, L., 2003, "Large Eddy Simulation Applied to a High Reynolds Flow Around an Airfoil Close to Stall," 41st AIAA Aerospace Sciences Meeting and Exhibit, Reno, NV, January 6–9.
[24] Shen, Y. Q., Zha, G.-C., and Wang, B. Y., 2008, "Large Eddy Simulation of Circular Cylinder Flow by Using High Order WENO Scheme," 38th Fluid Dynamics Conference and Exhibit, Seattle, WA, June 23–26.
[25] Chapman, D. R., 1979, "Computational Aerodynamics Development and Outlook," AIAA J., **17**(12), pp. 1293–1313.
[26] Shen, Y., and Zha, G.-C., 2010, "Large Eddy Simulation Using a New Set of Sixth Order Schemes for Compressible Viscous Terms," J. Comput. Phys., **229**, pp. 8296–8312.
[27] Dano, B., Kirk, D., and Zha, G.-C., 2010, "Experimental Investigation of Jet Mixing Mechanism of Co- Flow Jet Airfoil," 5th AIAA Flow Control Conference, Chicago, IL, June 28–July 1, Paper No. AIAA-2010-4421.